Transport in Porous Media **47:** 195–214, 2002.

Double-Diffusive Finger Convection in a Hele–Shaw Cell: An Experiment Exploring the Evolution of Concentration Fields, Length Scales and Mass Transfer

SCOTT E. PRINGLE[1,2], ROBERT J. GLASS[2] and CLAY A. COOPER[3]
[1]*Department of Civil Engineering, University of New Mexico, Alb., NM, U.S.A.*
[2]*Flow Visualization and Processes Laboratory, Sandia National Laboratories, Alb., NM, U.S.A.*
[3]*Division of Hydrologic Sciences, Desert Research Institute, Reno, NV, U.S.A.*

(Received: 9 August 2000; in final form: 6 June 2001)

Abstract. We present the results of an experiment conducted to explore the temporal and spatial development of double-diffusive finger convection in a Hele–Shaw cell. Two solutions each containing a different density affecting component were layered in a density stable configuration (sucrose solution over a more dense salt solution) with a nearly perturbation-free interface between. The mismatch of diffusive time scales for the two components leads to local density instabilities that generate upward and downward convecting fingers. Throughout the course of the experiment, a full-field quantitative light transmission technique was used to measure concentration fields of a dye tracer dissolved in the salt solution. Analysis of these fields yielded the temporal evolution of length scales associated with the vertical and horizontal finger structure as well as mass transfer. Distinct developmental stages are identified with strong correlation between all measures. These data provide a baseline that can be used to develop and evaluate both process-level models that simulate the full complexity of the evolving flow field and large-scale effective models that integrate over small-scale behavior.

Key words: double-diffusive convection, instability.

1. Introduction

When multiple density-affecting components are present in a fluid, their dissimilar diffusion can lead to the development of a wide range of convective structures resulting from local hydrodynamic instabilities (see reviews by Turner, 1973, 1974, 1985). Such convection, referred to as double-diffusive (two components) or multi-component (three of more components), develops features that are much different from those associated with stable advective, dispersive, and/or diffusive processes, and can significantly increase mass transfer rates. While considered to be an important mixing process in the world's oceans (with salt and heat as the components), it is widely recognized that such convection can also occur in porous media (Nield, 1968; Green, 1984; Imhoff and Green, 1988), and has become a topic

of research with respect to the potential movement of contaminants in subsurface environments.

Numerical simulations can contribute valuable insight into the behavior of double-diffusive systems (Shen and Veronis, 1991; Chen and Chen, 1993; Shen, 1995; Shen and Veronis, 1997; Stockman *et al.*, 1998). However, to properly constrain such investigations, laboratory experiments are required. There are a variety of methods that have been used in the laboratory to obtain data in three-dimensional fluid tanks and porous media. Conductivity probes have been applied to obtain vertical salinity profiles (e.g. Turner, 1967; Taylor and Veronis, 1996). Removal of a small amount of fluid at specified locations has also been a common approach to determine fluid concentrations and density variations (e.g. Linden, 1973; Griffiths and Ruddick, 1980; Imhoff and Green, 1988). Additionally, optical methods including polarimetry (Lambert and Demenkow, 1971) and absortometry (Kazmierczak and Poulikakos, 1989) have been used to obtain vertical concentration profiles. While each of these methods have provided data that has greatly increased our understanding of the double-diffusive process, they result in a limited number of data points within the entire flow field. Furthermore, some are intrusive and disrupt the natural evolution of the fluid motion. Because of this, it should come as no surprise that detailed quantitative experimental data to support numerical simulation is lacking (Kazmierczak and Poulikakos, 1989; Shen and Veronis, 1991).

In this study, we use a non-intrusive light transmission technique that allows for point-wise concentration measurements of a dye tracer over the entire flow field ($\sim 2 \times 10^6$ data points) at relatively high spatial (~ 0.015 cm) and temporal (< 1 s) resolution in a Hele–Shaw cell. This technique has been applied in layered solutal systems to study the theoretical stability boundary for double-diffusive finger convection in Rayleigh parameter space (Cooper *et al.,* 1997) and more recently the temporal evolution of such fingering as a function of initial system dis-equilibrium (Cooper *et al.,* 2001). However, these experiments were initiated by physically removing a divider that separated the two solutions, resulting in an ambiguous initial condition that makes data interpretation and comparison to numerical simulation less than optimal. Here, the method of solution layering is modified to yield a well defined, nearly unperturbed interface between the two solutions at the start of the experiment. The high-resolution concentration fields of the resulting double-diffusive fingering are analyzed to yield horizontally averaged, vertical concentration profiles from which representative process-induced vertical length scales as well as mass transfer are measured in time. Additionally, concentration field analysis allows us to quantify the temporal evolution of a corresponding horizontal length scale at the position of the initial solution interface.

2. Experimental Design

To provide an unobstructed view of the evolving fluid motion, we designed our experiment in a transparent Hele–Shaw cell using the common sodium chloride

Table I. Initial fluid properties and Rayleigh numbers

ΔT (kg/kg)	0.03436 (+/−0.00007)
ΔS (kg/kg)	0.05234 (+/−0.00010)
β_T	−0.6892 (+/−0.0034)
β_S	−0.3719 (+/−0.0018)
D_T ($m^2\ s^{-1}$)	1.477×10^{-09} (+/− 2.2×10^{-11})
D_S ($m^2\ s^{-1}$)	4.878×10^{-10} (+/− 9.7×10^{-12})
D^a_{dye} ($m^2\ s^{-1}$)	5.670×10^{-10} (+/− 1.1×10^{-11})
υ_T ($m^2\ s^{-1}$)	1.033×10^{-06} (+/− 2.1×10^{-08})
υ_S ($m^2\ s^{-1}$)	1.125×10^{-06} (+/− 2.2×10^{-08})
R_T	26,460(+/− 800)
R_S	21,579 (+/− 650)

[a]From Detwiler *et al.* (2000).

(T) and sucrose (S) solutes with Lewis number, $\mathrm{Le} = D_T/D_S$, of 3.03, where D_T and D_S are the molecular diffusion coefficients of sodium chloride and sucrose, respectively. The fluid configuration is such that a layer of less dense sucrose solution overlies a layer of more dense sodium chloride (salt) solution, in a near step function configuration. The dimensionless buoyancy ratio, $R_\rho = \beta_T \Delta T/\beta_S \Delta S$, is near neutral buoyancy at 1.22, where $\beta_T = -(1/\rho_o)(\partial\rho/\partial T)$ and $\beta_S = -(1/\rho_o)(\partial\rho/\partial S)$ are the volumetric expansion coefficients (Nield and Bejan, 1992), and ΔT and ΔS are the initial concentrations of the salt and sucrose solutions, respectively. The dimensionless solutal Rayleigh numbers, with permeability included in the scaling of viscous influences, are defined as $R_T = \beta_T \Delta T g H k/D_T \upsilon$ and $R_S = \beta_S \Delta S g H k/D_T \upsilon$, where g is the gravitational acceleration in the plane of the cell, H is the cell height, k is the intrinsic permeability, and υ is the mean kinematic viscosity of the fluid.

Table I gives the initial solution property values used in this study. The volumetric expansion coefficients were calculated based on linear regression of the density versus concentration data from Weast (1986) between 0 and the initial concentration of each solution. The molecular diffusion coefficients for sodium chloride and sucrose were obtained from Stokes (1950) and Irani and Adamson (1958), respectively, at 50% of their maximum concentration representing levels within the initial solution interface (the mixed zone between the upper and lower solutions). The viscosities, based on the solution concentrations, were obtained from Weast (1986). Figure 1 shows the location of the experiment in solutal Rayleigh space.

The Hele–Shaw cell was fabricated from two polished glass plates that were separated by plastic shims along their long axis edges and clamped together at the shims within an aluminum frame. The cell was placed onto a test stand (Figure 2) with a controlled output light source (Sylvania F30 T12 fluorescent bulbs with Mercron FX16144-4 controllers) and a CCD camera (Princeton Instruments

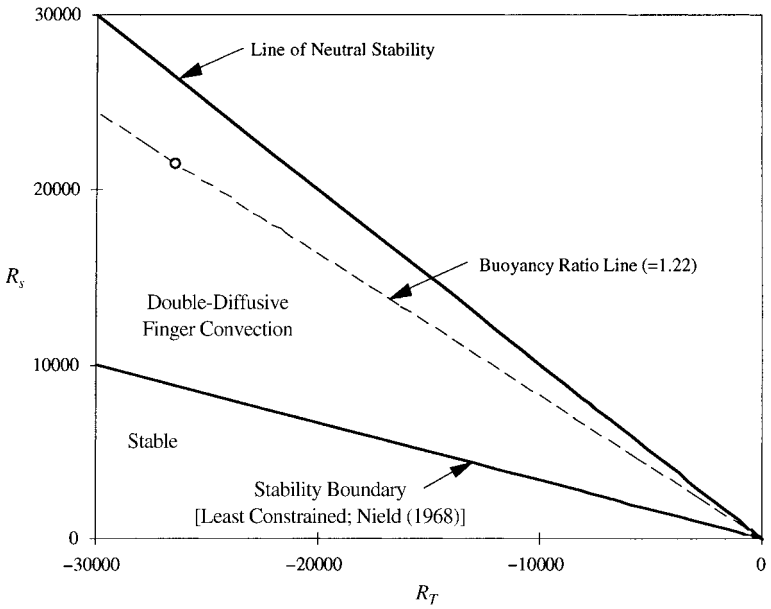

Figure 1. Location of the experimental point (circle) within Rayleigh parameter space with an R_ρ value of 1.22.

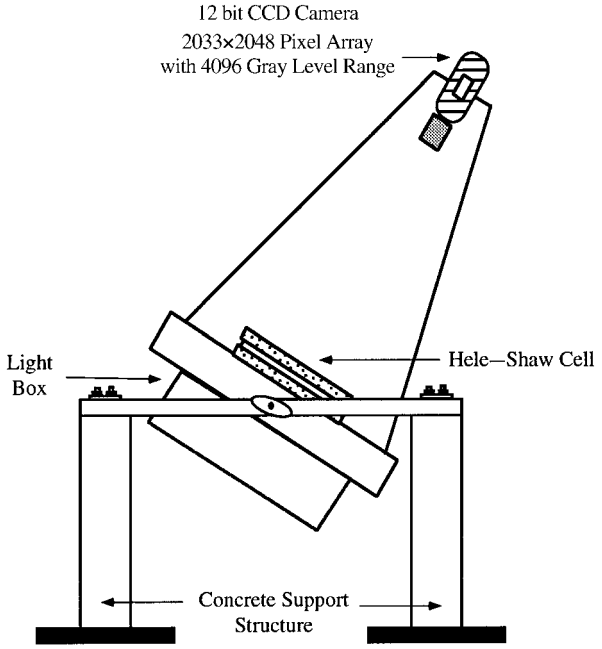

Figure 2. Schematic illustrating the light transmission system. The Hele–Shaw cell was placed onto the test stand at 65° from vertical. A CCD camera detects light transmitted through the aperture of the Hele–Shaw cell. The dimensions of the structure are ~4.5 m high with a distance between concrete supports of ~1.5 m.

Table II. Hele–Shaw cell dimensions and measured aperture statistics

Dimensions, cm × cm	25.41 (length) × 16.25 (height)
Dimensions (pixel × pixel)	1055 × 1650
Pixel size, cm	1.54×10^{-2}
Minimum aperture, cm	1.72×10^{-2}
Maximum aperture, cm	1.81×10^{-2}
$\langle b \rangle$[a], cm	1.77×10^{-2}
σ_b, cm	1×10^{-4}
k, cm^2	2.61×10^{-5}
σ_k, cm^2	1×10^{-7}
RMS error[a], % of mean	0.8

[a]Method described in Detwiler *et al.* (1999).
σ represents the standard deviation.

TEA/CE-2033 detector with an array of 2033 × 2048 pixels each with 4096 gray levels) to measure the light intensity field transmitted through the Hele–Shaw cell. A Kodak Red #25 filter was added to the camera lens to limit the range of wavelengths measured to those absorbed most effectively by the dye dissolved in the salt solution. A diffuser plate located between the cell and the bulb housing improved the spatial uniformity and ensured a diffuse light source. Temperature was monitored at a number of locations along the surface of the Hele–Shaw cell and showed only a small variation in time and space (21.7 +/− 0.2°C). The angle of the cell relative to vertical (65°) was defined, after the concentration was chosen and intrinsic permeability was measured, in order to give the desired Rayleigh numbers (see Table I).

Table II summarizes the dimensions and relevant measured statistics of the Hele-Shaw cell aperture field. The aperture field was determined using the method of Detwiler *et al.* (1999) and shows a narrow distribution ($\sigma_b = 1.0 \times 10^{-4}$ cm) about its mean ($\langle b \rangle = 0.0177$ cm). Semivariograms for the x and z direction (long and short principal axes, Figure 3(a)) show trends along the short and long axis of the Hele–Shaw cell. These trends are caused primarily by the clamping pressures applied along the long edges of the glass plates and result in larger apertures at the centerline of the cell (0.0181 cm) and smaller apertures at the extreme cell edges (∼0.0172 cm) (see Figure 3(b)). The intrinsic permeability was calculated using the relationship $\langle b \rangle^2/12$ (Bear, 1988) yielding a value of 2.61×10^{-5} cm^2.

Numerous techniques have been applied to layer a lighter over a heavier solution, with the most common being a physical divider placed into a gap between the glass plates. However, such dividers can leak, and additionally when removed, allow a viscous boundary layer at the upper and lower surface to develop creating vortices and inducing a long wavelength disturbance within the fluid (Cooper *et al.,* 1997, 2001; Dalziel *et al.,* 1999). These artificial perturbations can influence the ensuing fluid motion and make data interpretation difficult. To minimize initial

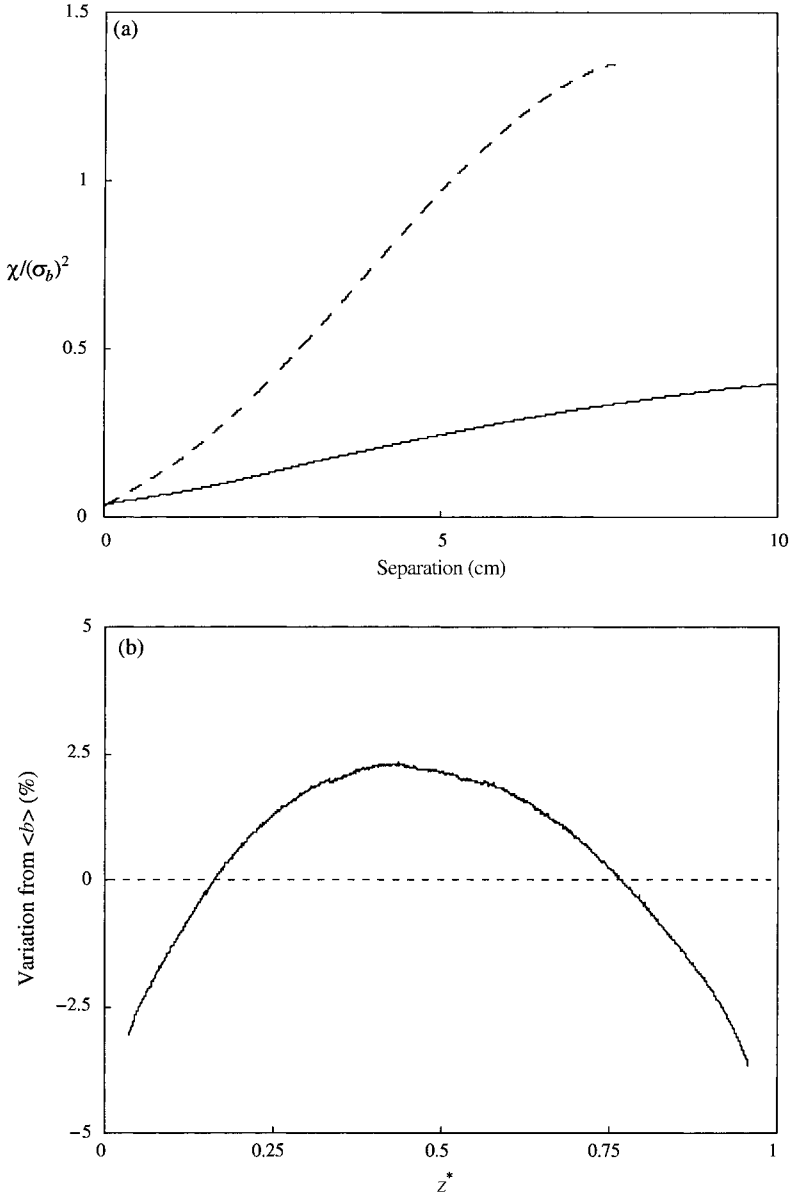

Figure 3. Hele–Shaw cell aperture field characterization. (a) Semivariogram, normalized by the variance $(\sigma_b)^2$, for the x (solid line) and z (dashed line) direction (long and short principle axes, respectively) of the Hele–Shaw cell aperture field. (b) Variation from the mean aperture across the short principle axis (z-direction) of the cell, $z^* = z/H$ ($z^* = 0$ signifies the top horizontal boundary). The clamping pressures along the top and bottom edges of the glass plates cause a slight aperture variation; at the extreme cell edges (<3 mm), optical effects led to erroneous measurements.

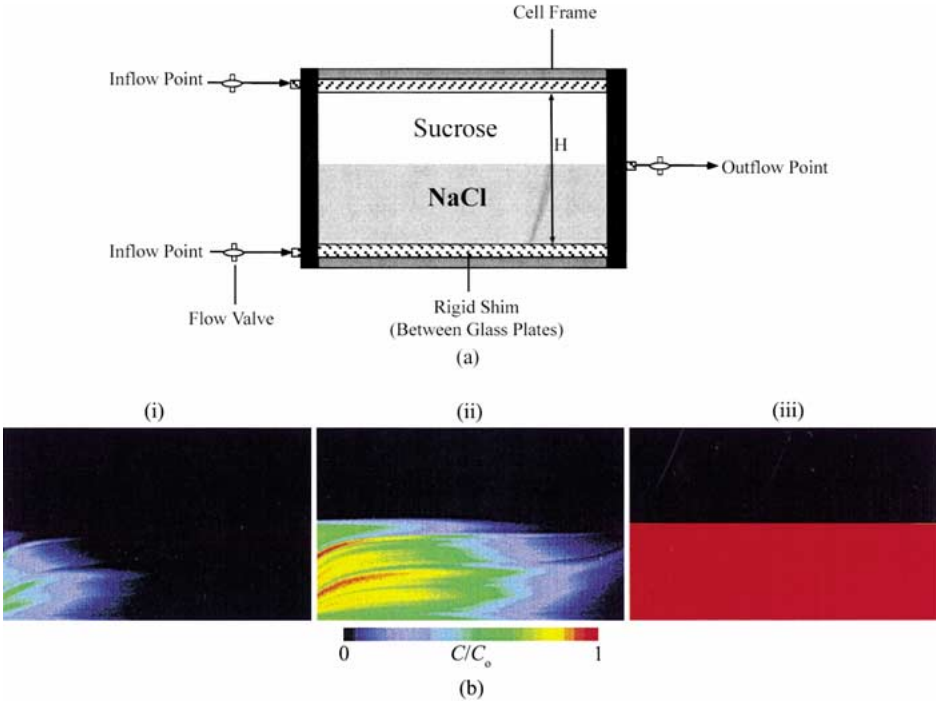

Figure 4. Illustration of initial solution layering. (a) Schematic of Hele–Shaw cell with two inflow and single outflow port locations and the initial configuration of a layer of sucrose over a denser salt solution. The aluminum frame contacts the glass plates only along the long edges. (b) Series of concentration fields are shown from left to right at $t \sim 2$ s, $t \sim 4$ s, and $t \sim 10$ min after the start of solution flushing. Dyed salt solution and undyed sucrose solution enter from the lower and upper corners of the left side, respectively, and exit at the center of the right side, forming an initial solution interface ~0.102 +/− 0.002 cm thick (with less dense sucrose solution (black) over more dense salt solution (red)). Total flushing time prior to the start of the experiment was ~ 30 min (100 pore volumes). Hele–Shaw cell dimensions are 25.41 cm (length) × 16.25 cm (height) with a 0.0177 cm gap.

perturbations, we developed a technique to fill the cell that results in a uniform, near disturbance-free interface between the two solutions (Figure 4(a), (b)). The cell was first saturated with water, and then the solutions (dyed salt and un-dyed sucrose) were flushed through the cell from the upper and lower corners at one side and out through the center at the opposite side. After ~100 cell volumes of each solution were flushed, the inflow and outflow valves were closed, and the instability was allowed to evolve naturally from the rest state. Analysis of the initial solution interface using single pixel-wide vertical transects across the cell yielded a mean interface thickness of ~0.1 cm.

A dye tracer (Warner Jenkins FD&C Blue #1) at a concentration of 0.25 g/kg was mixed with the salt solution to allow visualization and quantification of the convective motion; the addition of dye had a negligible influence on the fluid density. The measured concentration fields are those of the dye with salt concentration

inferred (i.e. dye/salt). The salt has a diffusivity approximately 2.5 times that of the dye, and therefore, the dye does not map the salt perfectly; however, since the motion is convective throughout much of the experiment, the diffusivity difference should have only a small impact on this mapping.

Light intensity images were transformed into concentration fields normalized by the maximum initial concentration (C/C_o) using a calibration curve obtained from a series of dye concentrations (0–0.25 g/l with steps of 0.05) in a base salt solution equal to that used in the experiment (method described by Detwiler *et al.*, 2000). In the remainder of the paper, we refer to C/C_o simply as concentration. Over the course of an experiment, the mass balance error systematically increased resulting in a maximum error of 5% by the end of the experiment. Subsequent tests revealed that this error was due to the interaction of salt, sucrose and dye. We compensated for this mixing effect by applying a correction function of the form $(C/C_o)_{new} = 1+\varphi(\sin[\pi C/C_o]_{old})$, where φ is a coefficient based on the maximum error in mass balance at the end of the experiment, $(C/C_o)_{old}$ is the concentration obtained from the calibration curve, and $(C/C_o)_{new}$ is the corrected concentration. After applying this function point wise within each field, mass balance error was within 0.5% throughout the course of the experiment with a maximum RMS error at any location in the field of 0.014.

3. Results

A total of 300 images of the evolving concentration field were taken at predetermined time intervals ($\sim$20 s at early time and $\sim$10 min at late time) throughout the course of the 16 h experiment. A sequence of concentration fields are shown in Figure 5 chosen based on the percent of the initial dye/salt mass transferred upward across the centerline of the cell (from 1% in Figure 5(a) to 51% in Figure 5(l)). In the following sections we first describe the evolution of the concentration field and then present quantitative measures of system behavior. Throughout the rest of the paper, we present time as dimensionless ($t^* = tD_T/H^2$) based on the dimensionless governing equations in Nield and Bejan (1992).

3.1. DESCRIPTION OF THE EVOLVING INSTABILITY

Starting from the rest state, instability is first detected at t^* of 7.83×10^{-6}, and the growing perturbations quickly organize into an array of distinct fingers that rapidly grow in unison (see magnified C/C_o sequence in Figures 6(a), (b)). At t^* of $\sim 2.34 \times 10^{-5}$, the fingers begin to interact with one another causing a re-organization of the initial uniform finger structure (Figures 6(c), (d)). Figure 5(a) and its magnification in Figure 6(d) (t^* of 4.03×10^{-5}) show the concentration field near the end of the re-organization or 'transition' period to be composed of a large number of very small fingers with a wide variation in vertical extent. As convection proceeds, small-scale fingers continuously emerge from the region of

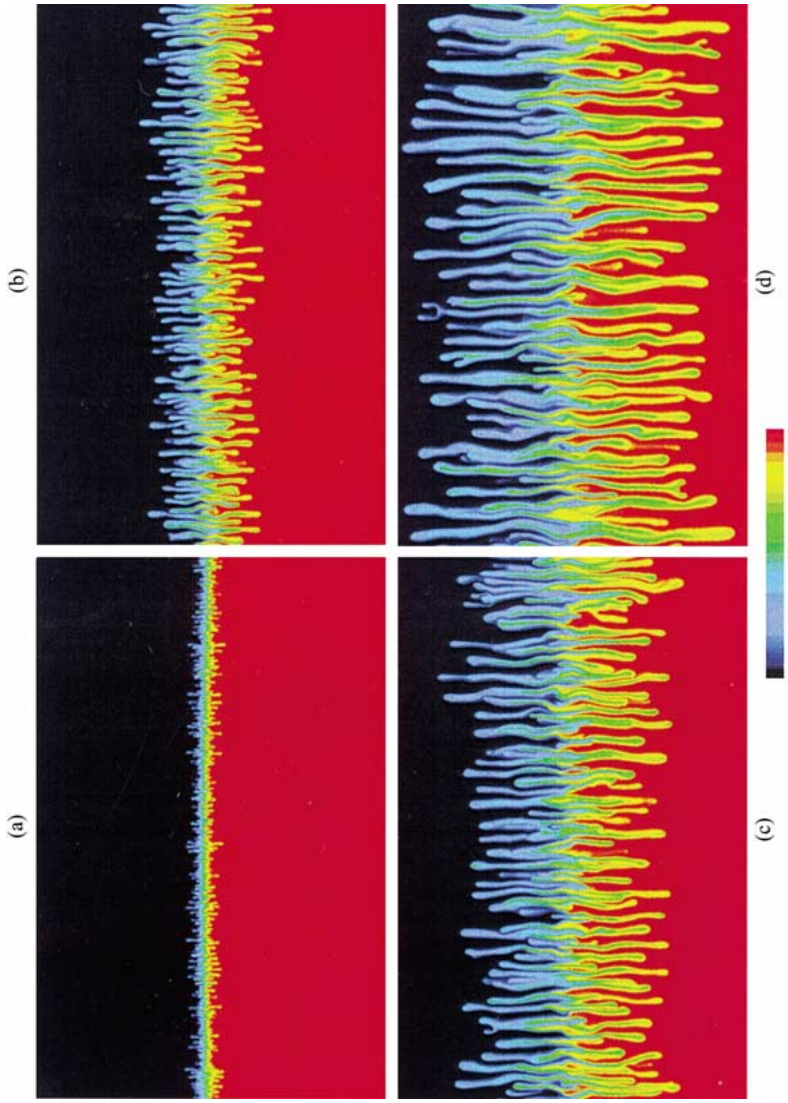

Figure 5. Series of concentration fields (25.41 cm × 16.25 cm) at (a) $M^* = 0.01, t^* = 4.03 \times 10^{-5}$, (b) $M^* = 0.05, t^* = 1.31 \times 10^{-4}$, (c) $M^* = 0.1, t^* = 2.21 \times 10^{-4}$, (d) $M^* = 0.15, t^* = 3.22 \times 10^{-4}$, (e) $M^* = 0.20, t^* = 4.23 \times 10^{-4}$, (f) $M^* = 0.25, t^* = 5.24 \times 10^{-4}$, (g) $M^* = 0.30, t^* = 6.04 \times 10^{-4}$, (h) $M^* = 0.35, t^* = 7.25 \times 10^{-4}$, (i) $M^* = 0.40, t^* = 7.85 \times 10^{-4}$, (j) $M^* = 0.45, t^* = 1.03 \times 10^{-3}$, (k) $M^* = 0.50, t^* = 1.77 \times 10^{-3}$, and (l) $M^* = 0.51, t^* = 3.17 \times 10^{-3}$. Color sequence black–blue green–yellow–orange–red depicts normalized concentration from 0 to 1. Notable features discussed in text.

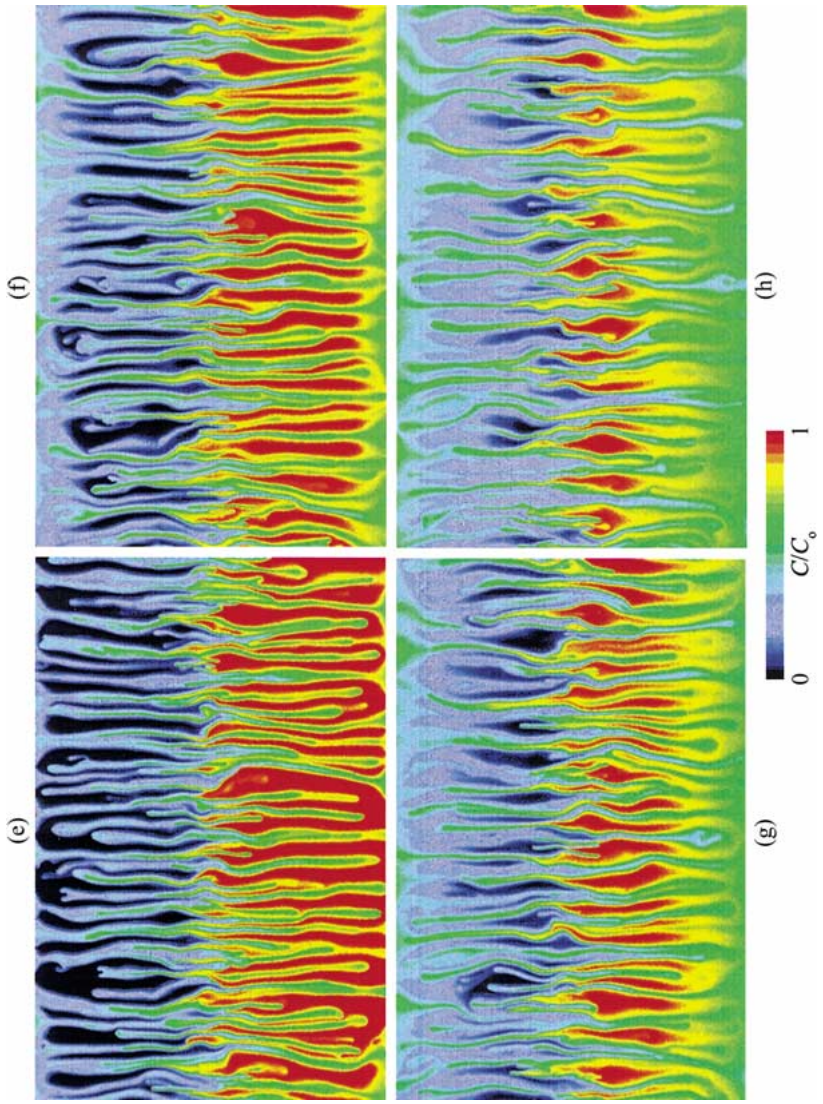

Figure 5. (continued)

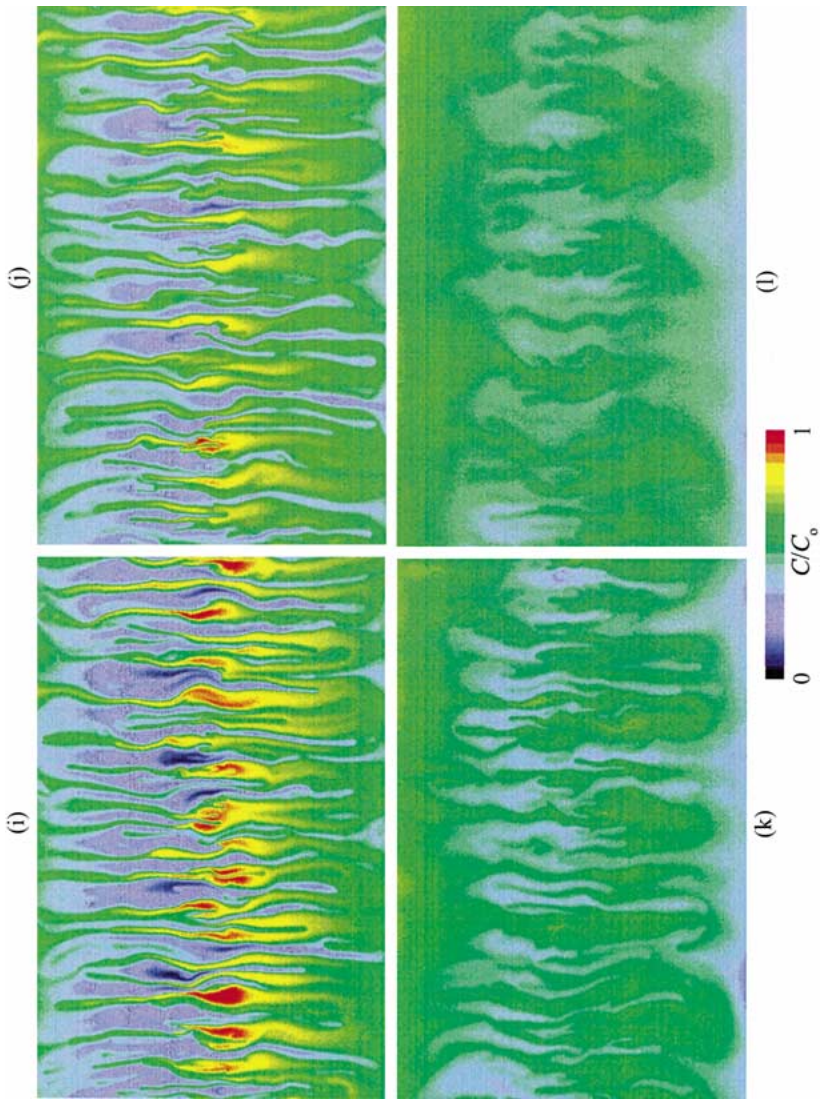

Figure 5. (continued)

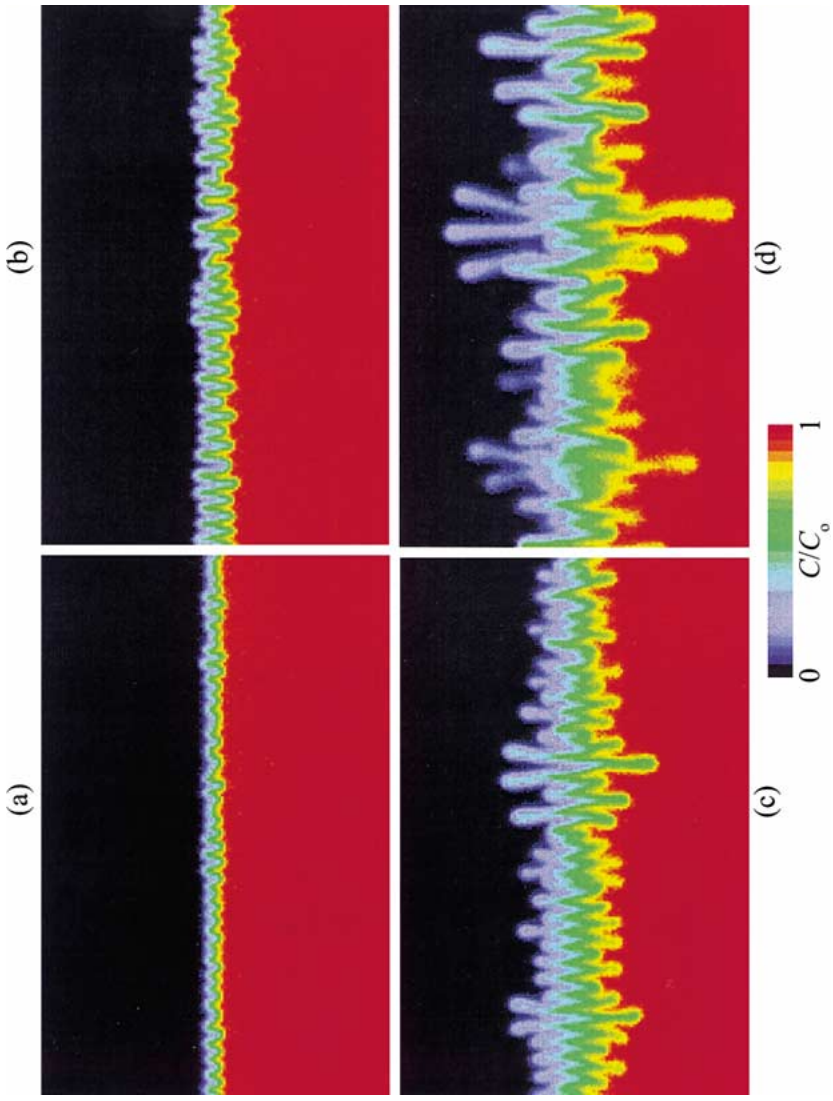

Figure 6. Series of magnified concentration fields (3.2 cm × 2 cm) during the early stage (a) $M^* = 0.0007$, $t^* = 7.83 \times 10^{-6}$, (b) $M^* = 0.0022$, $t^* = 1.12 \times 10^{-5}$, (c) $M^* = 0.007$, $t^* = 2.34 \times 10^{-5}$, (d) $M^* = 0.01$, $t^* = 4.03 \times 10^{-5}$. Color sequence black–blue–green–yellow–orange–red depicts normalized concentration from 0 to 1. Notable features discussed in text.

the initial solution interface referred to as the 'finger generation zone' by Cooper *et al.* (2001). These newly generated fingers add to the structural intricacy of the field by growing, and in many cases, merging with, and convecting up through the stems of earlier formed neighbors. The generation of new finger pairs at the tips of some upward and downward growing fingers is also observed (Figure 5(c)–(f)). At t^* of 4.23×10^{-4} (Figure 5(e)), the fastest growing fingers reach the top and bottom boundaries of the cell and begin to spread laterally forming more dense (at the bottom) and less dense (at the top) 'clouds' of fluid. Figures 5(f)-(h) show the clouds extending toward the center of the cell. Within the finger generation zone, far from the boundaries, new fingers continue to form from isolated pockets of nearly pristine solution located about the initial solution interface (Figure 5(g)–(j)). Finally, at late time, the finger structure becomes 'tree-like' with a branching pattern that has greater lateral travel than at early time. This final convective structure remains long after motion has stopped, diffusion now acting to slowly uniformize the field (Figure 5(l)).

3.2. QUANTITATIVE MEASURES OF SYSTEM BEHAVIOR

Concentration fields are horizontally averaged to yield vertical profiles as shown in Figure 7. By choosing an upper and lower concentration on each profile (C/C_o

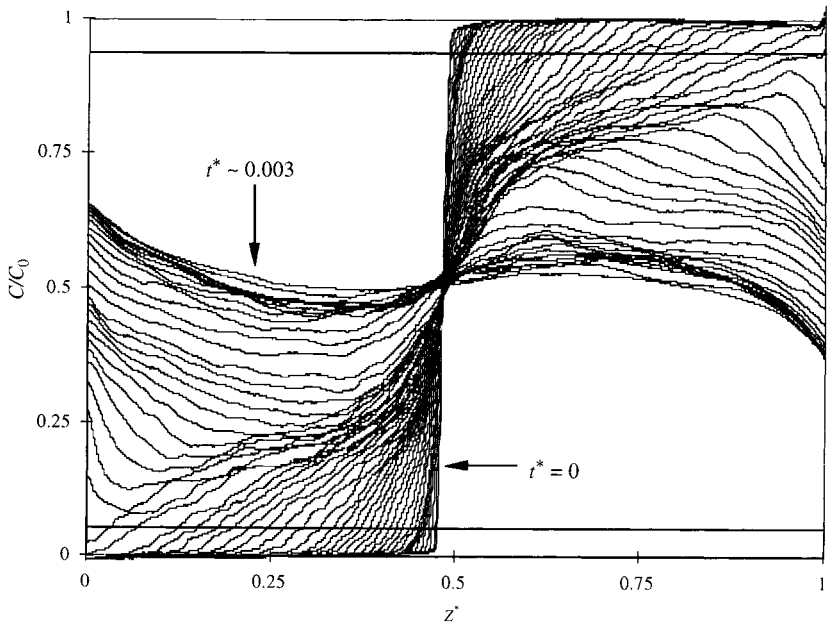

Figure 7. Horizontally averaged concentration as a function of vertical position, $z^* = z/H$ ($z^* = 0$ is the top horizontal boundary). Tracking the translation of set concentrations in time (see lines for constant C/C_0 of 0.05 and 0.95) allows the definition of an evolving vertical length scale.

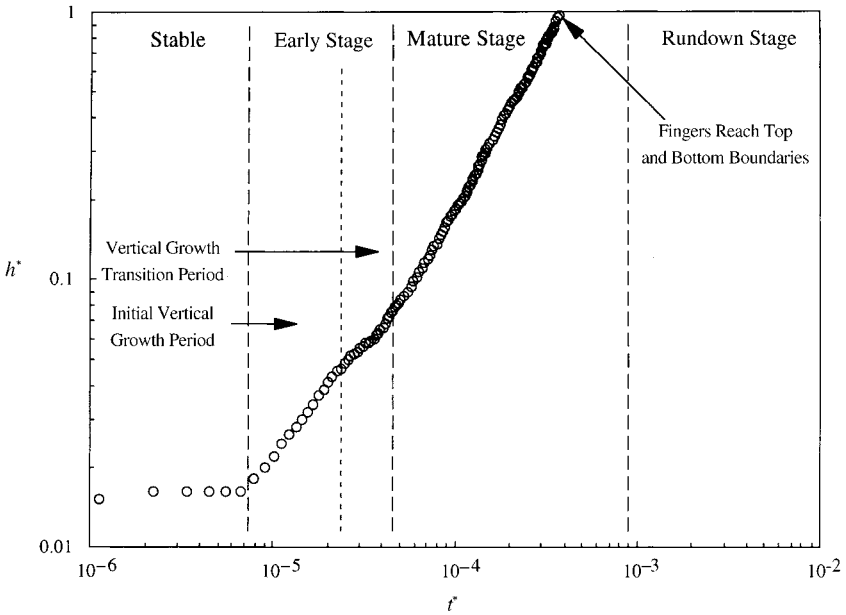

Figure 8. Normalized vertical length scale, $h^* = h/H$, as a function of time showing regions of steady growth (see first part of the early stage and the mature stage) separated by a non-steady growth transition region. The instability onset occurs at t^* of $\sim 8 \times 10^{-6}$. The data at $h^* = 1$ ($t^* \sim 4 \times 10^{-4}$) signifies contact of the fingers with the top and bottom boundaries of the cell after which our definition of h soon becomes undefined.

$= 0.95$ and 0.05), we can define a vertical length scale, h, representative of the evolving finger structure, as the distance between the chosen concentrations. Considering the normalized vertical length scale, h^* ($= h/H$), as a function of time, reveals a number of distinct developmental stages (Figure 8). After the onset of instability, the first or early stage begins with a linear increase of h^* followed by the transition period where its growth slows and convection reorganizes. The next or mature stage is defined where h^* growth resumes its linear increase in time. The characteristic dimensionless vertical velocity, $V_c^* = V_c H/D_T$, obtained from regression of the linear increase in h^* during the mature stage is $\sim$2400. Such linear behavior has been commonly reported for both solute–heat and solute–solute systems in viscous fluids (e.g. Linden 1973; Taylor and Veronis, 1996), porous media (Imhoff and Green, 1988) and Hele-Shaw cells (Cooper *et al.*, 2001). However, the early time variation shown here has in many cases been overlooked or not detected by the measurement method applied. After fingers have reached the top and bottom boundaries at t^* of 4.23×10^{-4}, h becomes undefined as concentration profiles invert at their ends (Figure 7). The vertical lines in Figure 8 represent the approximate boundaries between distinct developmental stages, including a rundown stage (as will be defined below), and are shown on all remaining plots for reference.

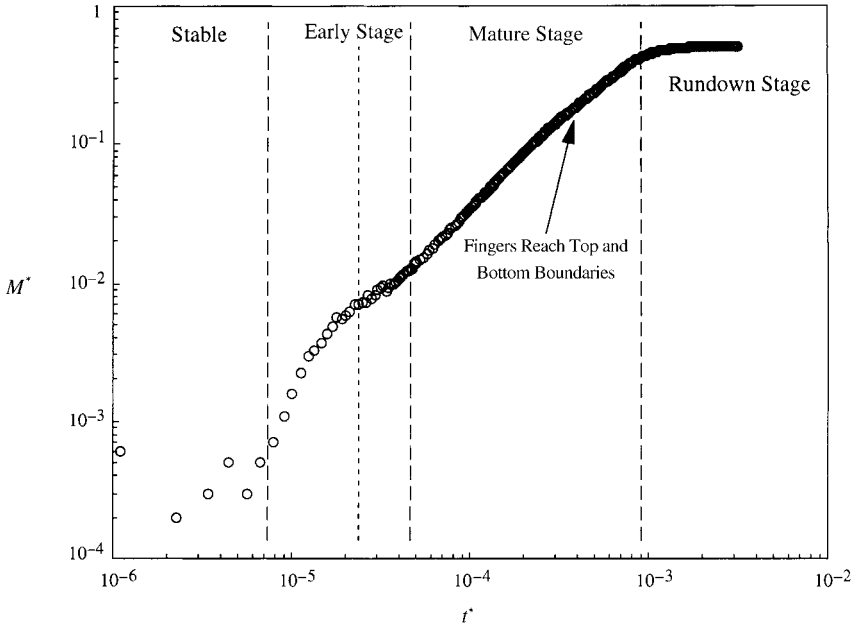

Figure 9. Normalized mass transfer of dye/salt, $M^* = M/M_o$, upward across the centerline of the cell as a function of time showing similar trends as in Figure 8. The mass transfer rate is uninfluenced by the initial contact of the fastest convecting fingers with the top and bottom boundaries.

An arithmetic average of the concentration profile data gives the normalized mass transfer of dye/salt, M^* $(= M/M_o)$, upward across the center line of the cell in time, where M_o is the total dye/salt mass in the cell (Figure 9). Applying a five-point central difference scheme to this data results in estimates of the mass transfer rate. The corresponding normalized mass transfer rate, Q_m^* $(= M^*/t^*)$, in time, is shown in Figure 10 (represented by crosses). The fluctuation in the data is far above that due to error in the concentration measurements and is the result of the complex unstable convective process itself. The rate data can be further smoothed to more clearly reveal the temporal trend (Figure (10), circles), showing a constant Q_m^* of 23.0 during the mature stage followed by a power law decay that we use to define the final or rundown stage. Note that the early time transition period where the growth rate of h^* decreases (see Figure 8), corresponds well to a decrease in mass transfer in the same period (Figure 10). This sinusoidal response in the mass transfer rate during the early stage was also observed in the simulations of Shen and Veronis (1991).

A representative horizontal length scale, λ, can also be defined by dividing the cell length by the number of concentration swings (upward and downward pairs) along a horizontal traverse of the cell. We note that this measure could be thought of as twice an average finger width, and must also recognize it to yield different results depending on the vertical position where the traverse is made. Taking the

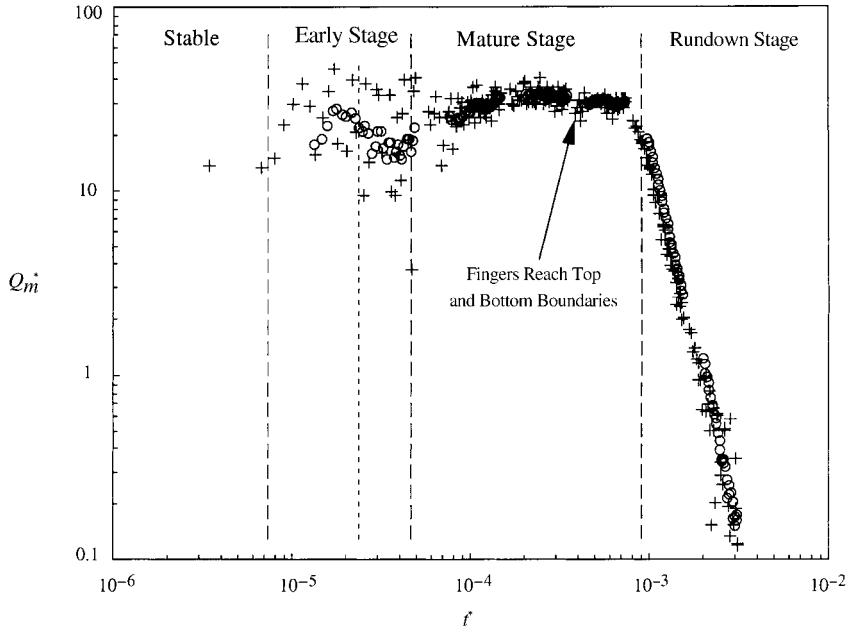

Figure 10. Normalized mass transfer rate of dye/salt, $Q_{\mathrm{m}}^* = M^*/t^*$, upward across the centerline of the cell as a function of time. A five-point central difference applied to the mass transfer data in Figure 9 shows significant fluctuation in the data (represented by crosses), and an additional 10 point moving average on the rate data reveals trends more clearly (represented by circles).

position to capture the finger generation zone at the centerline of the cell, we plot a normalized horizontal length scale, λ^* ($= \lambda/H$), as a function of time in Figure 11. At early time, fingers grow in vertical extent only and thus λ^* is initially constant. When the vertical growth slows due to convective reorganization (see transition period in Figure 8), λ^* increases (Figure 11). At the beginning of the mature stage, the growth of λ^* slows, then as time proceeds, once again increases. For the final period of the mature stage, data shows a power law relationship in time with an exponent of 0.57. The experimental work by Cooper *et al.* (2001) for Rayleigh numbers of order 100,000 (based on the cell height) and R_ρ ranging from 1.4 to 2.8, yielded an exponent of $\sim$0.5. However, we note that even though the overall growth of the horizontal length scale is reasonably represented with a power law in time, we see fluctuations, again indicative of the complex unstable convective process (Figure 11).

4. Discussion of Experimental Limitations

Using a transparent Hele–Shaw cell to investigate double-diffusive convection allows us to resolve the structural patterns that form because it provides a clear, unobstructed view of the double–diffusive fingers as they develop that is difficult

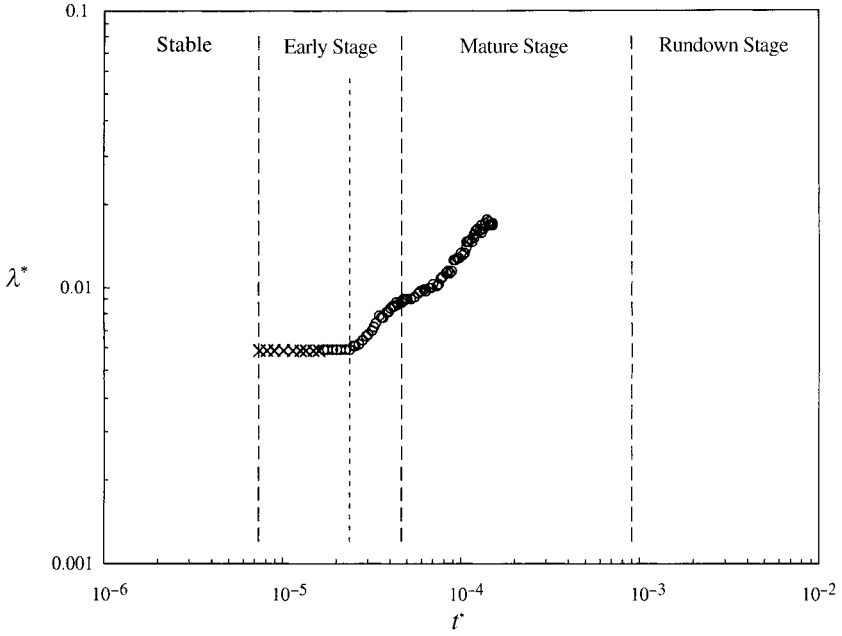

Figure 11. Normalized horizontal length scale, $\lambda^* = \lambda/H$, as a function of time. For $t^* < 2 \times 10^{-5}$, measurements were made by eye (represented by diagonal crosses), after which an analysis code was applied (represented by circles). For $t^* > 2.0 \times 10^{-4}$ no data are presented because the increasingly diffuse nature of the concentration swings within the finger generation zone lead to inaccurate measurements.

to achieve in real or artificial porous media. The Hele–Shaw cell also provides an analog for flow through porous media if the following assumptions are satisfied (Wooding, 1960):

$$\frac{\langle b \rangle}{\delta} \ll 1, \qquad \frac{V_c \langle b \rangle^2}{\delta \upsilon} \ll 1, \qquad \frac{V_c \langle b \rangle^2}{\delta D} \ll 1, \tag{1 a–c}$$

where δ is the smallest length scale of motion (taken to be the horizontal length scale), and D the diffusivity of the slowest component. The first criterion (1a) requires the smallest length scale of motion to be much larger than the mean aperture. This criterion was satisfied within several minutes after the start of the experiment. The second criterion (1b) requires inertial effects to be negligible relative to viscous effects, and this criterion was satisfied throughout the experiment. The third criterion (1c) requires the momentum transfer across the gap to be negligible relative to diffusive transfer. After onset, this criterion is exceeded, implying that the concentration fields contain a gradient in the third dimension (across the gap). In preliminary numerical simulations using a lattice-Boltzmann approach, recognition of the three-dimensional nature of the field has been shown to influence concentration field evolution (Stockman *et al.*, 1998). However, beyond the simple criteria in 1(a–c), other factors exist in porous media that make it intrinsically

different from a Hele–Shaw cell such as the presence of dead end pores, microporosity within grains, pore scale flow path tortuosity, and ever present heterogeneity and anisotropy, all of which could cause deviation in behavior between the two systems.

Finally, we note that to quantify the observed behavior, dye was introduced into the salt solution and assumed to behave passively, that is, to travel in the convective flow field and not undergo motion of its own. This assumption is justified through the mature stage by calculations of the Peclét number ($\mathrm{Pe} = V_c h / D_{\mathrm{dye}}$) within a finger, where V_c is the dimensional characteristic velocity and D_{dye} is the diffusivity of the dye in water. For our experiment, $V_c \sim 10^{-4}$ cm s^{-1}, $D_{\mathrm{dye}} \sim 10^{-6}$ cm^2 s^{-1}, and $h \sim 10$ cm, yielding Pe$\sim 10^3$. However, the dye will not fully map the salt at longer times during system rundown when diffusion begins to dominate.

5. Conclusion

The behavior of double-diffusive finger convection has been investigated in a transparent Hele–Shaw cell using a light transmission technique that provides high-resolution concentration fields. From a near perturbation-free initial layering of a lighter sucrose solution over a denser salt solution, upward and downward moving fingers quickly form at the interface between the two solutions. After the onset of fingering, the temporal evolution of length scales representative of the vertical and horizontal finger structure as well as mass transfer are characterized by three developmental stages: early, mature, and rundown. The vertical length scale during the early stage increases steadily, experiences a transition where vertical growth slows, then, during the mature stage, resumes a steady increase. The mass transfer rate shows a sinusoidal response during the early stage, transitioning to constant behavior during the mature stage and power-law decay after rundown begins. The horizontal length scale is initially constant during the early stage, then steadily increases through the transition period, slows as the mature stage is entered, and then once again increases. These results show correlation between quantitative measures relative to each distinct developmental stage and illustrate the type of observations that can be obtained from the data.

The data presented here provide a baseline for use in the development and evaluation of numerical models. There are two types of models that must be developed. The first type, which could be thought of as a ‘process level’ model, is formulated at the scale of the experiment in order to simulate the full complexity of the evolving flow field. Once evaluated, process level models can be extended to consider more than two density-affecting components as well as precipitation/reaction mechanisms that will also influence local fluid composition and density. The second type, an ‘effective level’ model, is formulated at larger scales and must capture the essence of the enhanced mass transfer in an effective large-scale sense. While necessary for regional-scale hydrogeological analyses where it is impossible to resolve the fine-scale structures as seen here, such an effective

level model will be a challenge to develop and will require additional fundamental understanding of the double-diffusive fingering process.

Acknowledgements

This research was supported by the U.S. Department of Energy's Basic Energy Sciences Geoscience Research Program under contract numbers DE-AC04-94AL85000 (Sandia National Laboratories) and DE-FG03-96ER14611 (Desert Research Institute). S. E. Pringle further acknowledges support from the Geoscience Center at Sandia National Laboratories and CAC from the Division of Hydrologic Sciences at the Desert Research Institute. Experiments were conducted at the Flow Visualization and Processes Laboratory at Sandia National Labs. A special thanks to Anthony Chavez for his work in constructing the light transmission stand and Mark Haagenstad for his assistance in fabricating the Hele–Shaw cell. Finally, we thank Curtis Oldenburg and three anonymous reviewers for their constructive criticism of the manuscript. All data presented in this paper, including an animation of the evolving concentration fields, are available and can be obtained from the authors.

References

Bear, J.: 1988, *Dynamics of Fluids in Porous Media*, Dover.

Chen, F. and Chen, C. F.: 1993, Double-diffusive fingering convection in a porous medium, *Int. J. Heat Mass Transfer* **36**, 793–807.

Cooper, C. A., Glass, R. J. and Tyler, S. W.: 1997, Experimental investigation of the stability boundary for double-diffusive finger convection in a Hele–Shaw cell, *Water Resour. Res.* **33**(4), 517–526.

Cooper, C. A., Glass, R. J. and Tyler, S. W.: 2001, Effect of buoyancy ratio on the development of double-diffusive finger convection in a Hele–Shaw cell, *Water Resour. Res*. **37**(9), 2323–2332.

Dalziel, D. B., Linden, P. F. and Youngs, D. L.: 1999, Self-similarity and internal structure of turbulence induced by Rayleigh–Taylor instability, *J. Fluid Mech.* **399**, 1–48.

Detwiler, R. L., Pringle, S. E. and Glass, R.J.: 1999, Measurement of aperture fields using transmitted light: an evaluation of measurement error and their influence on simulations of flow and transport through a single fracture, *Water Resour. Res.* **35**(9), 2605–2617.

Detwiler, R. L., Rajaram, H. and Glass, R. J.: 2000, Solute transport in variable-aperture fractures: an investigation of the relative importance of Taylor dispersion and macrodispersion, *Water Resour. Res.* **36**(7), 1611–1625.

Imhoff, P. T. and Green, T.: 1988, Experimental investigation of double-diffusive groundwater fingers, *J. Fluid Mech.* **188**, 363–382.

Irani, R. R. and Adamson, W.: 1958, Transport processes in binary liquid systems. I. Diffusion in the sucrose-water system at 25°, *J. Phys. Chem*. **62**, 1517–1521.

Green, T.: 1984, Scales for double-diffusive fingering in porous media, *Water Resour. Res.* **20**, 1225–1229.

Griffiths, R. W. and Ruddick, B. R.: 1980, Accurate fluxes across a salt–sugar finger interface deduced from direct density measurements, *J. Fluid Mech.* **99**, 85–95.

Kazmierczak, M. and Poulikakos, D.: 1989, Transient double-diffusive convection experiments in a horizontal fluid layer extending over a bed of spheres, *Phys. Fluids A*. **1**(3), 480–489.

Lambert, R. B. and Demenkow, J. W.: 1971 On the vertical transport due to fingers in double diffusive convection, *J. Fluid Mech.* **54**, 627–640.

Linden, P. F.: 1973, On the structure of salt fingers, *Deep-Sea Res.* **20**, 325–340.

Nield, D. A. 1968, Onset of thermohaline convection in a porous medium, *Water Resour. Res*. **4**, 553–560.

Nield, D. A. and Bejan, A.: 1992, *Convection in Porous Media*, Springer-Verlag.

Shen, C. Y. and Veronis, G.: 1991, Scale transition of double-diffusive finger cells, *Phys. Fluids A* **3**, 58–68.

Shen, C. Y.: 1995, Equilibrium salt-fingering convection, *Phys. Fluids* **7**, 707–717.

Shen, C. Y. and Veronis, G.: 1997 Numerical simulation of two-dimensional salt fingers, *J. Geophys. Res.* **102**, 23131–23143.

Stockman, H. W., Glass, R. J., Cooper, C. and Rajaram, H.: 1998, Accuracy and computational efficiency in 3D dispersion via lattice-Boltzmann: models for dispersion in rough fractures and double-diffusive convection, *Int. J. Modern Phys. C* **9**, 1545–1557.

Stokes, R. H.: 1950, The diffusion coefficients of eight univalent electrolytes in aqueous solution at 25°, *J. Am. Chem. Soc*. **72**, 2243–2247.

Taylor, J. and Veronis, G.: 1996 Experiments on double-diffusive sugar–salt fingers at high stability ratio, *J. Fluid Mech.* **321**, 315–333.

Turner, J. S.: 1967, Salt fingers across a density interface, *Deep-Sea Res.* **14**, 599–611.

Turner, J. S.: 1973, *Buoyancy Effects in Fluids*, Cambridge, 368 pp.

Turner, J. S.: 1974, Double-diffusive phenomena, *Ann. Rev. Fluid Mech*. **6**, 37–56.

Turner, J. S.: 1985, Multicomponent convection, *Ann. Rev. Fluid Mech*. **17**, 11–44.

Weast, R. C.: 1986, *CRC Handbook of Chemistry and Physics*, 66th edn., CRC Press, Boca Raton, Fla.

Wooding, R. A.: 1960, Instability of a viscous liquid of variable density in a vertical Hele–Shaw cell, *J. Fluid Mech.* **7**, 501–515.